UC Berkeley
UC Berkeley Previously Published Works

Title
Topological localization in out-of-equilibrium dissipative systems

Permalink
https://escholarship.org/uc/item/5rd236t5

Journal
Proceedings of the National Academy of Sciences of the United States of America, 115(39)

ISSN
0027-8424

Authors
Dasbiswas, Kinjal
Mandadapu, Kranthi K
Vaikuntanathan, Suriyanarayanan

Publication Date
2018-09-25

DOI
10.1073/pnas.1721096115

Peer reviewed

Topological localization in out-of-equilibrium dissipative systems

Kinjal Dasbiswas[a,b], Kranthi K. Mandadapu[c,d], and Suriyanarayanan Vaikuntanathan[a,e,1]

[a]The James Franck Institute, The University of Chicago, Chicago, IL 60637; [b]Department of Physics, University of California, Merced, CA 95343; [c]Department of Chemical and Biomolecular Engineering, University of California, Berkeley, CA 94720; [d]Chemical Sciences Division, Lawrence Berkeley National Laboratory, Berkeley, CA 94720; and [e]Department of Chemistry, The University of Chicago, Chicago, IL 60637

In this paper, we report that notions of topological protection can be applied to stationary configurations that are driven far from equilibrium by active, dissipative processes. We consider two physically disparate systems: stochastic networks governed by microscopic single-particle dynamics, and collections of driven interacting particles described by coarse-grained hydrodynamic theory. We derive our results by mapping to well-known electronic models and exploiting the resulting correspondence between a bulk topological number and the spectrum of dissipative modes localized at the boundary. For the Markov networks, we report a general procedure to uncover the topological properties in terms of the transition rates. For the active fluid on a substrate, we introduce a topological interpretation of fluid dissipative modes at the edge. In both cases, the presence of dissipative couplings to the environment that break time-reversal symmetry are crucial to ensuring topological protection. These examples constitute proof of principle that notions of topological protection do indeed extend to dissipative processes operating out of equilibrium. Such topologically robust boundary modes have implications for both biological and synthetic systems.

topological protection | chiral active matter | stochastic networks | nonequilibrium fluctuations | dissipation

Theoretical and experimental studies of biophysical mechanisms, such as error correction in DNA replication (1), adaptation in molecular motors controlling flagellar dynamics (2–4), and timing of events in the cell cycle (5), are beginning to show the close connection between robust functioning and nonequilibrium forces. Theoretical results (6, 7) have also elucidated the connection between energy dissipation and fluctuations in a wide class of nonequilibrium systems and have shown how dissipation can be used to tune steady states of many-body nonequilibrium systems (8). However, unlike the behavior and characteristics of equilibrium systems, where no energy is dissipated, general principles governing fluctuations about a steady state or the steady state itself in far-from-equilibrium conditions are just being discovered. As such, strategies that allow for the engineering of specific robust steady states in nonequilibrium biological and soft matter systems are highly desirable. In this paper, we take an approach that is motivated by the physics of topological insulators to construct such states in nonequilibrium systems.

The discovery of robust localized edge states in mechanical systems (9) that resemble those found in topologically nontrivial electronic (10) and photonic (11) systems has enabled the development of new design principles. For instance, it has been shown that assemblies of coupled mechanical oscillators can support topologically protected directed modes at their boundary (12, 13). Such assemblies can function as waveguides robust to backscattering. Localized edge modes have also been discovered in mechanical lattices (9, 14). These edge modes can be set up either at the edge of a lattice (9) or at topological defects in the interior of the lattice (14). They are formally

zero-energy "free" modes but unlike the commonly found long-wavelength, zero-energy modes in the bulk of marginally stable lattices, these topologically protected boundary modes are highly resistant to perturbations due to disorder and environmental fluctuations. Like their electronic and photonic counterparts, topological modes in the above mentioned mechanical systems have been characterized by topological indices, such as winding or Chern numbers (15–17).

In this paper, we propose that topologically protected modes can be encoded in a variety of biological and soft matter contexts at the cost of energy dissipation. Topological protection can occur in non-Hermitian quantum models with dissipation (18, 19) or through time-periodic driving (20). We focus here on a very different class of driven dissipative classical systems that have no obvious topological properties. Like in the electronic and mechanical analogs, a topological index can be associated with the bulk of the system, which predicts protected zero or soft modes localized at the edge or an interface. The modes are highly robust and insensitive to perturbations. In all of the instances considered in this paper, topological protection and the presence of an associated tunable spectral gap require that the fundamental equations of motion contain dissipative couplings.

We derive our results in two broad and apparently dissimilar contexts. Both systems that we consider can be mapped to noninteracting model quantum Hamiltonians with topologically protected states using a procedure formally similar to that in ref. 9. In the first, we consider biochemical networks with connectivity motivated by those of networks commonly encountered in

---

Significance

Topological insulators and their analogs in mechanical materials support conducting states only on their surface. We show that such topologically protected edge modes can also occur as the steady states of classical systems driven out of equilibrium. As proof of principle of the generic applicability of such notions, we show the existence of topologically localized states in a collection of interacting particles described by a hydrodynamic theory and discuss a general procedure to establish them in stochastic networks. In both cases, dissipative processes that break time-reversal symmetry are key to topological protection. Our results provide design principles for robust edge modes in synthetic systems as well as for the localization of flow of matter and information in biology.

APPLIED PHYSICAL SCIENCES

biophysical information processing and control (21). We show that the spectrum of the master equation rate matrix can support localized edge modes that are separated from the bulk via a band gap. In the second, we consider a hydrodynamic description of active matter, specifically that of collections of driven rotating particles in a confined geometry on a frictional substrate (22, 23), that exhibit large-scale flow localized at the boundaries. The spectrum of dissipative modes in this context implies a rapid relaxation of fluctuations of the flow in the bulk, while edge states, including the stationary state, when allowed by boundary conditions, can be longer lived. This implication of topological protection in dissipative systems is distinct from the directed propagating edge modes described recently in fluids (24–26) that are more directly analogous to single-particle quantum models (10).

The hydrodynamic equations have a structure very different from that of master equations considered in the first example. The two address phenomena at very different length scales and timescales: one being a coarse-grained phenomenological description of disordered matter and the other being a microscopic approach involving a network of discrete states. Nonetheless, they both describe dissipative phenomena characterized by the production of entropy and lack time-reversal symmetry. Our results elucidate the design principles required for robust steady states in various biophysical and synthetic systems.

Topological Protection in Markov Networks

In this section, we consider the out-of-equilibrium statistical dynamics of stochastic processes described by a Markov network (27). Such descriptions are routinely used in statistical mechanics as reduced models of chemical and biophysical processes (28). For equilibrium systems, the steady states and dynamics of fluctuations about it can be described in terms of energy landscapes, but such a simple description is not available for out-of-equilibrium processes. Hence, any insight into the existence and robustness of steady states of systems driven out of equilibrium by energy-consuming processes, such as those involved in biological functions, is potentially valuable.

Here, we focus on the steady state of lower-dimensional networks characterized by uniform or nearly uniform transition rates between various mesoscopic states. This is in analogy with periodically ordered lattices in electronic and metamaterials that host localized topological states at their edges (10). We show in the following that the steady states of certain Markov networks can indeed be mapped onto the ground states of Su–Schrieffer–Heeger (SSH)-like models for 1D periodic systems with topological properties—the "forward" and "backward" transition rates in the master equation play the role of the hopping rates between the two sites of a unit cell in the SSH model (29).

A simple illustration of this is depicted in Fig. 1: the probability flow in a 1D Markov chain with constant rate of site-to-site transition rates in the bulk regions on the left and right of an interface separating them is shown in Fig. 1 *A* and *C*. By mapping the steady state of the 1D Markov chain to the ground state of a Hamiltonian of a topologically nontrivial tight binding model (Fig. 1 *B* and *D*), we show that a possibly "disordered" interface connecting two "bulk" regions of the network with different transition rates can host localized topological modes depending on the transition rates in the bulk. Our results follow from the bulk–boundary correspondence inherent in topological systems, where the existence of localized zero modes at an edge can be predicted by studying the properties of the system in the bulk (9).

The procedure for establishing the mapping between the stochastic process and the Hamiltonian of a topological tight binding model is distinct from and more direct than the previous work, in which we suggested that the properties of certain out-of-equilibrium Markov states can be understood in terms of
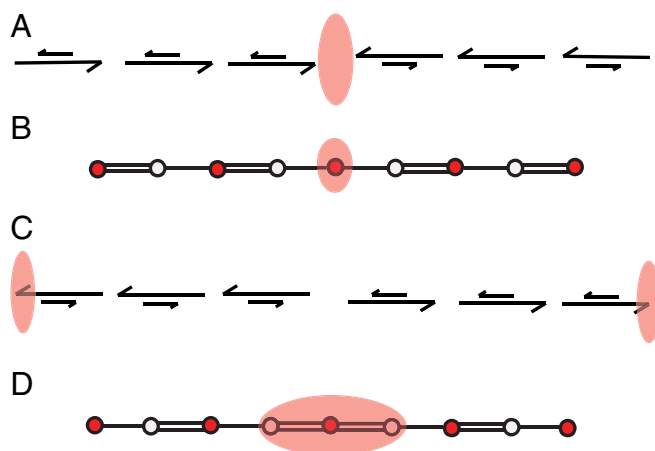

Fig. 1. Topological protection in a 1D out-of-equilibrium Markov-state network. *A* and *C* show 1D Markov networks with an interface: the transition rates are different in the left and right subregions of the network. *B* and *D* show corresponding lattices for the SSH model (9), with red and white sites representing two different sublattices. *A* shows the case when the net probability flow is toward the interface, leading to localization of the steady-state probability density there. *B* is the corresponding SSH lattice with an energy zero mode localized on the red site at the interface. *C* is when net probability flow is away from the interface, leading to localized probability density at either end of the chain. *D* is the corresponding SSH lattice with an energy zero mode localized on the white sites at the interface and on the red sites at the ends.

topological winding numbers (30). Indeed, we explicitly provide forms of tight binding Hamiltonians with ground states that are the steady states of the out-of-equilibrium stochastic processes that we consider. While the 1D network in Fig. 1 is fairly trivial, the procedure outlined below can be used to construct effective tight binding Hamiltonians for more complex biophysical networks with many cycles.

We begin by recalling that the dynamics of Markovian systems can be modeled using a master equation (28)

$$\frac{\partial \mathbf{P}}{\partial t} = \mathbf{W}\mathbf{P}, \qquad [1]$$

where the vector, $\mathbf{P}$, denotes the probability of occupancy of various distinct states (nodes in a Markov network). This is evolved in time by a transition matrix, $\mathbf{W}$, with elements W_{ij} indicating the rate of transition from state j to state i. The zero right eigenvector of the master equation, $|u\rangle$, specifies the steady state of the dynamics, which is necessarily unique for a finite connected Markov chain (28). We are interested in conditions under which this steady-state zero mode is localized at the interface. Formally, this requirement can be expressed as

$$\lim_{\epsilon \to 0} \mathrm{Tr} \frac{\epsilon \rho}{\mathbf{W} + \epsilon} = Tr[\rho|u\rangle \langle 1|], \qquad [2]$$

where ρ is a diagonal matrix with elements $\rho_i = 1$ for nodes i that are in the interfacial region and $\rho_i = 0$ otherwise. Here, $\langle 1|$ is the zero left eigenvector of the master equation, while the zero right eigenvector is denoted by $|u\rangle$. The trace in Eq. **2** counts the number of zero modes of $\mathbf{W}$ that are localized at the interfacial region (9). This is exactly equal to one if the unique steady-state solution, $|u\rangle$, is localized at this interface.

We now show that the condition in Eq. **2** can be related to a topological quantity calculated from the master equation in the bulk network. Note that the state to state transition matrix, $\mathbf{W}$, does not itself possess the symmetries usually associated with topological protection in electronic or mechanical materials

(10, 31). The eigenvalue spectrum of the master equation necessarily has one zero eigenvalue, with the rest of the eigenvalues being less than zero (28). Furthermore, $\mathbf{W}$ is usually nonhermitian and can have complex eigenvalues. In this form, Eq. **1** does not possess any obvious topological properties.

To uncover the topological properties of the master equation, we first note that the rate of change of probability can be expressed as (32)

$$
\frac{\partial \mathbf{P}}{\partial t} = \mathbf{W_0 J},
$$
$$
\mathbf{J} = \mathbf{W_1 P}, \tag{3}
$$

where the first is a continuity equation that expresses the conservation of probability with $\mathbf{W_0}$ being a discrete representation of the divergence operator and $\mathbf{J}$ is a vector of currents across each link in the network. The matrix $\mathbf{W_0}$ depends only on the topology of the network and not on the transition rates. The current vector, $\mathbf{J}$, can in turn be expressed in terms of the probability vector, $\mathbf{P}$, through the matrix $\mathbf{W_1}$, which depends on the transition rates in the network.

We are interested in cases when the trace count as described by Eq. **2** predicts the existence of localized zero modes. We will show below with concrete examples that Eq. **2** can be expressed as a topological invariant by using the fact that the information about the interface between two homogeneous bulk subregions is contained in $\mathbf{W_1}$ and not $\mathbf{W_0}$.

As an illustration of these steps, we first consider the 1D Markov chain in Fig. 1. The dynamics of the random walker can be described by the master equation in Eq. **1**. Using the above-mentioned decomposition into $\mathbf{W_0}$ and $\mathbf{W_1}$, we will show that the steady-state properties of the 1D random walker can map onto those of the well-known SSH model (9, 29). The central argument is that, if $\mathbf{W_1}$ has a zero right eigenvector, this eigenvector is the unique right eigenvector of $\mathbf{W}$ and hence, the steady state accessed by dynamics under $\mathbf{W}$. The topological properties of the zero eigenstate of $\mathbf{W_1}$ can be inferred by constructing the Hermitian matrix

$$
\mathbf{H} = \begin{pmatrix} 0 & \mathbf{W_1} \\ \mathbf{W_1^T} & 0 \end{pmatrix} \tag{4}
$$

and considering the trace

$$
\lim_{\epsilon \to 0} \mathrm{Tr}\left[\epsilon \sigma_3 \rho \frac{1}{\mathbf{H} + \epsilon} \right] = \delta n, \tag{5}
$$

where $\sigma_3 \equiv \begin{pmatrix} 1 & 0 \\ 0 & -1 \end{pmatrix}$ is the Pauli z matrix. The trace in Eq. **5**, denoted by δn, is the difference in the number of zero modes of $\mathbf{W_1}$ and $\mathbf{W_1^T}$ that are localized in the interfacial region. Since $\mathbf{W_1}$ is constrained by the properties of the master equation to have only 1 zero eigenvector, the trace in Eq. **5** can only take values $\delta n \in \{-1, 0, 1\}$. The steady state is localized at the interface between the two bulk regions when $\delta n = 1$, as shown in Fig. 1A, whereas it is localized at the opposite ends when $\delta n = -1$, as shown in Fig. 1C. The decomposition into $\mathbf{W_0}$ and $\mathbf{W_1}$ and the existence of localized steady states shown in Fig. 1 A and C for the 1D random walker are shown in detail in *SI Appendix*.

That δn in Eq. **2** can be expressed as a difference of integer topological winding numbers characteristic of the left and right bulks, $\nu_{L/R}$, is well-established through an index theorem in the context of electronic and mechanical topological lattices (9). Systems with $\delta\nu \equiv |\nu_L - \nu_R| \neq 0$ have zero modes that are topologically protected and resistant to perturbation. These arguments show that the steady state of the master equation $\mathbf{W}$ is localized and topologically protected whenever $\mathbf{W_1}$ is topologically nontrivial.

The topological winding numbers for the 1D random walker can be derived by considering the transition matrix in one of the bulk regions $\mathbf{W}^{\mathrm{b}}$:

$$
\mathbf{W}^{\mathrm{b}} = \mathbf{W_0^{\mathrm{b}}} \cdot \mathbf{W_1^{\mathrm{b}}} = \begin{pmatrix} 1 & -1 & & \\ & 1 & -1 & \\ & & \ddots & \ddots \\ & & & \ddots \end{pmatrix} \cdot \begin{pmatrix} \ddots & & & \\ \ddots & \ddots & & \\ & & w & -v \\ & & & w & -v \end{pmatrix}, \tag{6}
$$

where w and v denote rates of forward and back hopping in the bulk. In Eq. **6**, $(W_0^{\mathrm{b}})_{i,j} = \delta_{i,j} - \delta_{i+1,j}$ is a discrete representation of a gradient operator that encodes the topology of the network, while $(W_1^{\mathrm{b}})_{i,j} = -v\delta_{i,j} + w\delta_{i-1,j}$ depends on the hopping rates. Because of the repeated nature of these matrices corresponding to the periodicity of the Markov chain, they can be diagonalized in the bulk in a Fourier basis, $|k\rangle$, and represented as $\mathbf{W_0^{\mathrm{b}}} = \Sigma_k (1 - e^{-ik})|k\rangle\langle k|$ and $\mathbf{W_1^{\mathrm{b}}} = \Sigma_k(-v + we^{ik})|k\rangle\langle k|$, where the lattice constant is taken to be unity. The winding number of the bulk region can be obtained from the Fourier representation. Specifically, the bulk Hermitian matrix $\mathbf{H}$ that we construct from $\mathbf{W}$ can also be diagonalized in a Fourier basis:

$$
\mathbf{H} = \begin{pmatrix} 0 & \mathbf{W_1} \\ \mathbf{W_1^\dagger} & 0 \end{pmatrix},
$$
$$
\implies H(k) = \begin{pmatrix} 0 & -v + we^{ik} \\ -v + we^{-ik} & 0 \end{pmatrix}. \tag{7}
$$

In the form of Eq. **7**, one can see that $\mathbf{H}$ is isomorphic to the Hamiltonian of the quantum SSH model with hopping rates $-v$ and w. Using the results obtained for the SSH model, the winding number ν for the bulk phase can be calculated as (9)

$$
\nu = \frac{1}{2\pi i} \int_0^{2\pi} dk \frac{d}{dk} \ln W_1(k). \tag{8}
$$

We have mapped the zero modes of the 1D Markov chain directly to those of a corresponding SSH model, with the backward and forward transition rates playing the role of the two hopping parameters in the tight binding model of the Hamiltonian. The polarization generated in a topologically nontrivial SSH model is simply related to current generated by the bias in the random walk model. In this sense, dissipation in the bulk of the random walk model plays a crucial role in the generation of localized states. In analogy with the SSH model, two connected chains with opposite polarizations of probability flux will naturally lead to an accumulation of probability at the interface as the system approaches steady state.

The Markov-state model in Fig. 1 does not possess multiple cycles. Such cycles can allow for feedback at the cost of energy dissipation and are features common to Markov-state representations of many out-of-equilibrium biophysical processes (3). To derive our results in the context of out-of-equilibrium stochastic models relevant for biological processes, we consider the minimal Markov-state model shown in Fig. 2A that was introduced in ref. 30. This ladder-like Markov network possesses two horizontal rails with transition rates l^U, r^U, with l^L and r^L denoting the leftward and rightward transition rates in the upper and lower rails, respectively. There are also upward and downward transition probabilities along each vertical rung of the ladder denoted by u and d, respectively.

The Markov-state model is composed of two translationally invariant bulk-like regions with an interface connecting them. Specifically, the rates of transitions in the bulk regions do not
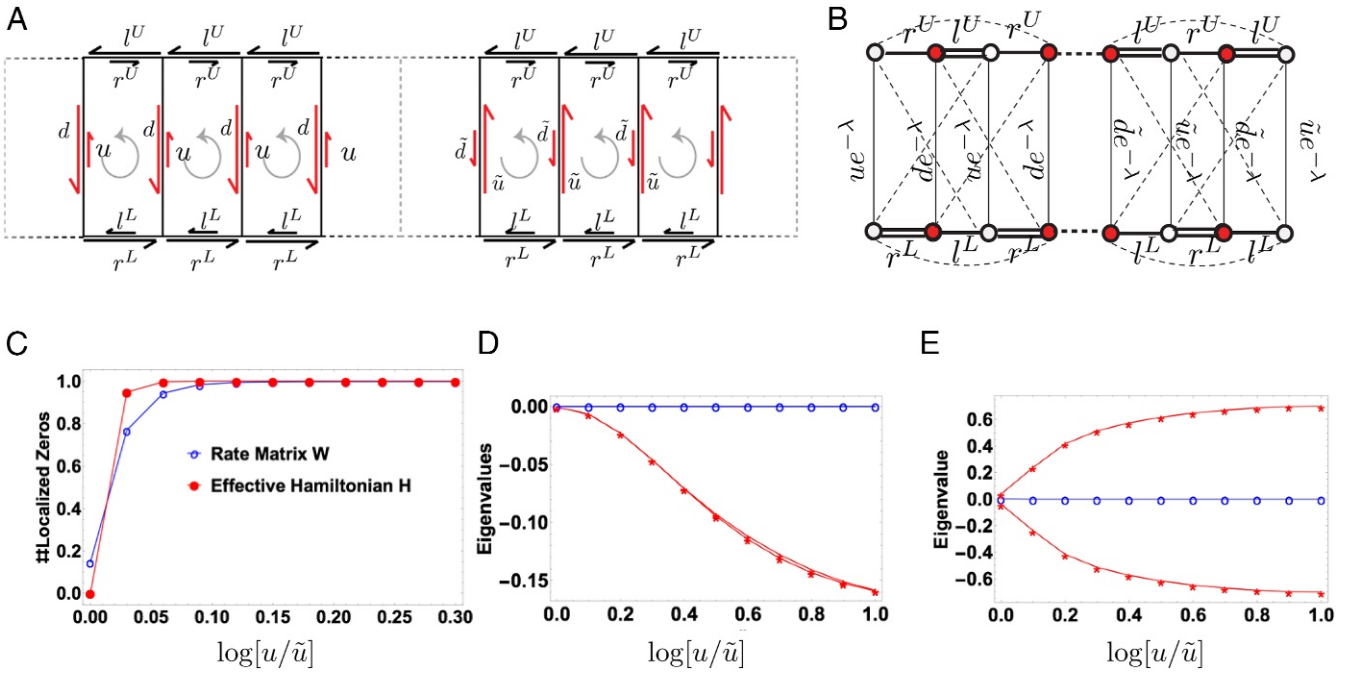
Fig. 2. Topological protection in a model out-of-equilibrium Markov-state network. (*A*) The ladder network with two coupled 1D Markov chains. The transition probabilities to go left, right, up, or down are labeled *l*, *r*, *u*, and *d*, respectively, to the left of the interface. The right bulk-like region is distinguished from the left by the different vertical transition rates $\tilde{u}$ and $\tilde{d}$, which lead to an opposite polarization on either side of the interface. The superscripts, *U* and *L*, denote the upper and lower rails of the ladder, respectively. (*B*) The analogous tight binding hopping model for electrons on a lattice. It involves higher-order couplings between next nearest neighbors (detailed expressions are in *SI Appendix*). (*C*) The number of localized zero modes calculated from the trace count in Eq. **2** for both the master equation (**W** for the ladder network) and the **H** operator obtained from it by the construction in Eq. **4**. (*D*) The first two eigenvalues of **W** showing that the eigenvalue gap closes when the transition rates are equal on the left and right subregions. (*E*) The corresponding first two eigenvalues of **H**. The plots in *C*–*E* are shown as a function of the inverse localization length, which is related to the ratio of vertical rates on either side of the interface: $u/\bar{u} = \tilde{v}/v$.

depend on the position along the horizontal axis. The rates in the interfacial region interpolate between the two bulk regions. The transition rates in the right bulk region are denoted by the (~) symbol to distinguish them from those on the left. As discussed in ref. 30, the spatial connectivity and structure of this Markov-state network resemble those of networks routinely used to study adaptation (4), kinetic proofreading (33, 34), and cell signal sensing (35). These and other Markov-state representations of biophysical processes can often be decomposed into bulk-like subgraphs stitched together by interfaces as indicated in Fig. 2*A*. The subgraphs are formed by finite periodic replication of a particular module or motif.

Since we are mainly interested in networks of the form in Fig. 2, which possess translational symmetry along one (horizontal) axis and the interface spans the other (vertical) axis, we decompose the rate matrix of this system as

$$\mathbf{W} = \mathbf{W}_0^x \mathbf{W}_1^x + \mathbf{W}_0^y \mathbf{W}_1^y, \qquad [9]$$

where $\mathbf{W}_{0/1}^{x/y}$ are square matrices and discrete representations of the continuity operator in the (horizontal) x and (vertical) y directions. Since the interface spans the vertical axis, we choose the decomposition

$$\mathbf{W} = \mathbf{W}_0^x (\mathbf{W}_1^x + (\mathbf{W}_0^x)^{-1} \mathbf{W}_0^y \mathbf{W}_1^y) \equiv \mathbf{W}_0^x \tilde{\mathbf{W}}_1^x. \qquad [10]$$

These arguments imply that any master equation rate matrix **W** can be factorized as $\mathbf{W} = \mathbf{W}_0^x \tilde{\mathbf{W}}_1^x$. For the ladder network, we consider the tilted version of the original master equation (36), $\mathbf{W}(\lambda)$ in Eq. **10**, because the bare $\mathbf{W}_0^x$ matrix is singular. The spectrum gap and topological conclusions are robust to the tilting

parameter λ (30). This decomposition and regularization scheme is explicitly shown in *SI Appendix*. Again, the crucial point in this decomposition is that $\mathbf{W}_0^x$ does not depend on the transition rates and possesses no interfaces. Using this property and arguments similar to the case of 1D random walk model, one can show that **W** has topologically protected modes whenever the following Hermitian operator constructed with $\tilde{\mathbf{W}}_1^x$ is topologically nontrivial:

$$\mathbf{H} = \begin{pmatrix} 0 & \tilde{\mathbf{W}}_1^x \\ (\tilde{\mathbf{W}}_1^x)^\dagger & 0 \end{pmatrix}. \qquad [11]$$

Like the master equation rate matrix, the Hamiltonian **H** is also composed of two bulk phases connected by interfaces. A schematic of the connections in the effective Hamiltonian is provided in Fig. 2. We provide the detailed derivation and explicit expression for **H** in *SI Appendix*.

The polarization implicit in the Hamiltonian **H** reflects the currents generated by the master equation rate matrix **W**. For instance, the effective Hamiltonian that we have depicted in Fig. 2*B* is composed of two horizontal rails, each with a lattice structure that resembles that of the SSH model. The two rails can potentially have polarizations with the same magnitude but opposite signs. This choice corresponds to the case $l^U = r^L$ and $r^U = l^L$. In such cases, the effective Hamiltonian can have a net polarization only when the vertical links connecting the two rails break symmetry. Indeed, this condition reflects the requirement that the symmetry between the two rails of the ladder in the master equation rate matrix be broken, $u \neq d$, for a current along the horizontal axis of the bulk networks. In this sense, topological protection depends crucially on the currents generated by the dissipative fluxes in the master equation rate matrix. In the context of the models considered here, systems without dissipative

Dasbiswas et al.

fluxes in their bulks cannot support a topologically protected mode. In Fig. 2C, we show the numerically computed count of localized zero eigenmodes of **W** using Eq. **2** and compare it with that of the effective matrix **H**. We also show the gaps in the eigenvalue spectrum for **W** and **H** in Fig. 2 C and D, respectively, by numerically computing the first two eigenvalues as the hopping rates are varied. Such a gap between the steady state and subsequent eigenvalues in the eigenvalue spectrum makes the steady state robust against random fluctuations. We indeed find that, as long as the Hamiltonian **H** has a winding number mismatch that supports a localized zero mode at the interface, **W** is also guaranteed to have a zero mode localized to the interface.

This correspondence between a master equation operator, **W**, and a topologically nontrivial Hamiltonian, **H**, is the main result of the first part of the paper. It establishes that the topological properties of **W** can be computed by simply constructing winding numbers for the matrix $\tilde{\mathbf{W}}_1^x$. This mapping allows us to infer the properties of a stochastic out-of-equilibrium system in contact with thermal reservoirs in terms of the topological properties of an isolated quantum mechanical system described by the Hamiltonian **H**. The Hamiltonian reflects the polarization of the bulk master equations that support a current. Importantly, a demonstration that the steady states of these nonequilibrium networks have a localized character allows us to comment on the gap between the steady-state zero eigenvalue of the master equation and the first negative eigenvalue. Recent work has shown that, given the same asymptotic steady-state distribution, Markov-state networks that preserve detailed balance always have spectral gaps lower than the spectral gaps of dissipative Markov-state networks that violate the condition of detailed balance (37, 38). A localized steady-state solution with a localization length scale can be obtained using transition rates derived from a potential energy landscape (i.e., rates that satisfy the principle of detailed balance). Since the timescales for relaxation generally increase as the localization length increases—the slowest relaxation timescale in a system with a truly delocalized steady-state solution diverges as a function of system size—the spectral gap of an equilibrium system with a finite localization length is nonzero. Such an estimate of the spectral gap then sets a bound on the gap of the corresponding nonequilibrium system. In this manner, our arguments can be used to prove the existence of both a localized solution and an associated band gap, two signatures of topologically protected states.

Topological Protection in Many-Body Systems

There is broad interest in dissipative, steady-state structures (such as ordered phases and topological defects therein) that emerge in collections of particles driven away from equilibrium in both synthetic (39, 40) and biological contexts (41, 42). Such steady states, if topologically protected, are likely to be robust against disorder and can be categorized into distinct topological classes—thus guiding applications that involve organization away from equilibrium (8, 43).

The results of the previous sections are, however, specific to effectively single-particle Markov-state processes. A natural question is whether similar statements about topological modes can be made for collections of many interacting particles out of equilibrium. Indeed, an effective Markov-state representation of the dynamics of a many-particle interacting system cannot be simplified in the same way as the models in Figs. 1 and 2. While a full microscopic description of a many-particle interacting system is in general intractable without performing detailed simulations, the relaxation of such a system toward equilibrium or a steady state can be described in terms of a few slowly decaying collective modes with long wavelengths. Such a hydrodynamic description in terms of long-wavelength collective modes differs fundamen-

tally from the electronic or mechanical materials with periodic order in which topologically protected edge states typically occur (9, 10).

As a nontrivial application of this notion of topological protection to a many-particle system, we focus on collections of actively rotating particles (rotors) with an intrinsic "spin" angular momentum degree of freedom (Fig. 3A). The collective dynamics of such particles are more complex and relatively less understood than those that involve linear self-propulsion (39), although there is now a wide range of experiments where such active angular momentum injection in the bulk can be realized in a controlled manner (23, 44). Examples of such chiral active flows include shaken chiral grains (22), liquid crystals in a rotating magnetic field (45), and light-powered colloids (46). Instances of naturally occurring flowing matter with actively generated rotation by molecular motors range from the rotational beating of flagella of swimming bacteria to active torque generation in the cellular cytoskeleton (47). Boundary flows where the rotors circulate around the edge of a container have been seen in ref. 22 and more recently in simulations in ref. 23. In a biological context, such flows have been implicated in the breaking of left–right symmetry during morphogenesis (48). However, connections to topological protection, if any, have not been explored. We now show that driven rotors in a finite 2D geometry on a dissipative substrate can indeed support topologically protected localized edge states. These states allow the
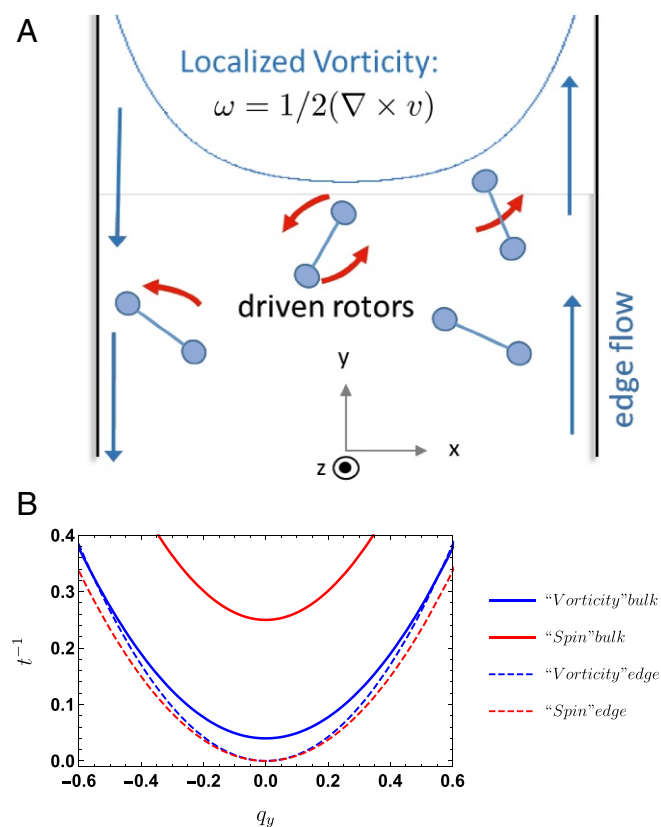

Fig. 3. Topological protection of hydrodynamic boundary modes. (A) Model of actively spinning rotors confined between two plane surfaces. (B) Bulk spectrum of inverse lifetimes of diffusive modes of the chiral active hydrodynamics (eigenvalues of the bulk operator are defined in Eq. **14**) along with their corresponding edge modes (dashed lines). The parameter values used are $D_S = D_T = 1.0$, $\lambda_\Omega = 1.0$, $\lambda_\omega = 5.$, $\rho = \mathcal{I} = 1.$, and $\Gamma = 0.1$ rescaled in terms of the relevant length scales and timescales, here chosen to be λ_Ω, as well as corresponding diffusion time, λ_ω^2/D_S.

system to robustly localize long-lived flows and fluctuations to its edge, while fluctuations in the bulk dissipatively decay over a finite lifetime set by friction. This topological interpretation of the hydrodynamic modes is the main result of this part of the manuscript.

Chiral Active Hydrodynamics: Flow and Fluctuations. The dynamics of a collection of actively spinning rotors can be described by a coarse-grained hydrodynamic theory formulated in terms of conservation laws and constitutive relations derived using the general principles of irreversible thermodynamics formulated in the seminal work of de Groot and Mazur (49). The key hydrodynamic variables in the theory are intrinsic rotation rate (or spin angular velocity) $\Omega(\mathbf{x}, \mathbf{t})$ and the linear flow velocity of the rotors $\mathbf{v}(\mathbf{x}, t)$, corresponding to the conservation of angular momentum and linear momentum, respectively. We assume incompressibility based on the observation that the density of rotors remains nearly uniform (23). The hydrodynamic equations corresponding to the complex rotor systems can be inferred using the principles of linear irreversible thermodynamics (49) from a dissipation functional

$$\mathcal{R} = \int d\mathbf{x} \left[\eta(\nabla \mathbf{v})^2 + D_\Omega(\nabla\Omega)^2 + \Gamma(\Omega - \omega)^2 + \Gamma_v v^2 + \Gamma_\Omega \Omega^2 \right],$$
[12]

which is derived from the proportionality of the thermodynamic forces and fluxes through the phenomenological dissipative coefficients: the spin–vorticity coupling Γ, the rotational diffusion constant D_Ω, the viscosity of the medium η, and the substrate friction coefficients for angular and linear velocities Γ_Ω and Γ_v, respectively. A crucial feature of these phenomenological equations of motion is the dissipative coupling between the angular velocity and the vorticity, $\omega = (\nabla \times \mathbf{v}(\mathbf{x}))_z/2$, through the rotational strain rate, $\Omega - \omega$ (50–52). These dissipative processes that contribute to the net rate of entropy production in Eq. **12** together with the uniform active torque, τ, driving each rotor determine the dynamics. We do not consider the theoretically allowed "odd viscosity," which is nondissipative and is important at high drive (53).

The coupled dynamical equations for the spin angular velocity, Ω, and vorticity, ω, are derived by extremizing the above dissipation functional (49), $\mathcal{R}$, as

$$\mathcal{I}D_t\Omega = D_\Omega(\nabla^2 - \lambda_\Omega^{-2})\Omega + \Gamma\omega + \tau,$$
[13]

$$\rho D_t\omega = (\eta + \Gamma/4)(\nabla^2 - \lambda_\omega^{-2})\omega - (\Gamma/4)\nabla^2\Omega,$$

where the total time derivative, $D_t \equiv \partial/\partial t + \mathbf{v}.\nabla$, includes the convective term and $\mathcal{I}$ is the moment of inertia density. The decay length scales are defined as $\lambda_\Omega^{-2} = (\Gamma + \Gamma_\Omega)/D_\Omega$ and $\lambda_\omega^{-2} = \Gamma_v/(\eta + \Gamma/4)$ as in ref. 22. The collection of spinning rotors driven by an active intrinsic torque, τ, in the presence of substrate friction, Γ_Ω, decays to a bulk steady state with angular velocity and vorticity given by: $\Omega_b = \tau/(\Gamma + \Gamma_\Omega)$ and $\omega_b = 0$ (22, 23).

In a confined geometry, the rotors are prevented from rotating freely at the walls, which induces a spatial profile in the angular velocity and therefore, in the vorticity (22, 23). In fact, a finite cluster of uniformly spinning unconfined rotors also exhibits edge vorticity. These steady-state solutions of the hydrodynamic theory are detailed in *SI Appendix*. Taken together, these hydrodynamic solutions illustrate for different boundary conditions that a steady-state flow can occur only at the edge of a finite system with substrate friction and not in the bulk, which has zero vorticity.

The dissipation-dominated dynamics (the convective term, being quadratic in velocity, is negligible for small flows or small-amplitude flow fluctuations) about the uniform steady state of

chiral active fluids, $\Omega \to \Omega - \Omega_b$, are described by $\partial_t|\Omega, \omega\rangle = -\mathbf{M}|\Omega, \omega\rangle$, where the linear dynamic operator, $\mathbf{M}$, is derivable from Eq. **13**. The bulk diffusive modes of the spin and vorticity fluctuations about the steady-state flow, Ω_b, are given in terms of the bulk 2D wavevector, $\mathbf{q} = q_x\hat{x} + q_y\hat{y}$, as

$$\frac{\partial}{\partial t}\begin{pmatrix}\Omega \\ \omega\end{pmatrix} = -\begin{pmatrix} D_S(q^2 + \lambda_\Omega^{-2}) & -\Gamma/\mathcal{I} \\ -\Gamma q^2/(4\rho) & D_T(q^2 + \lambda_\omega^{-2}) \end{pmatrix}\begin{pmatrix}\Omega \\ \omega\end{pmatrix},$$
[14]

where $D_S = D_\Omega/\mathcal{I}$ and $D_T = (\nu + \Gamma/4)/\rho$ are the diffusivities of spin and linear momentum. Since we consider purely dissipative processes, an excited collection of particles relaxes monotonically in time toward the steady state, which corresponds to minimal dissipation. The spectrum of $\mathbf{M}$ comprises the inverse relaxation timescales for decay of fluctuations about the bulk steady state, with the steady state itself as a zero eigenvector.

Topological Interpretation of Dissipative Hydrodynamic Modes. While $\mathbf{M}$ in itself has no apparent topological properties, its positive semidefinite character for purely dissipative dynamics allows us to construct a suitable square root $\mathcal{H}$, which may possess a nontrivial topological index (9), as we now show. In doing so, we are inspired by the example of Dirac (54) as well as of mechanical lattices (9, 31). Importantly, however, our objective in taking this square root is not to go from second-order (in time) to first-order dynamics but to construct topologically nontrivial operators.

In the regime of weak spin–vorticity coupling, $\Gamma \ll \eta$, the modes in Eq. **14** reduce to nearly independent spin and velocity fluctuations, with timescales of decay that are given by the eigenvalues of Eq. **14**. In the small q limit, these inverse decay times are proportional to $m_{\omega,\Omega}(q) \sim q^2 + \lambda_{\omega,\Omega}^{-2}$. The corresponding simple linear differential operator, $\nabla^2 - \lambda^{-2}$, effectively governs the spin and vorticity fluctuations. Here, λ is a length scale used to represent either of $\lambda_{\omega,\Omega}$. To interpret it topologically, we map to a single-particle quantum model by taking its square root:

$$\mathcal{H} = \begin{pmatrix} -i\partial_y & -\partial_x + m \\ \partial_x + m & i\partial_y \end{pmatrix}$$
$$= m\hat{\sigma}_1 - i\partial_x\hat{\sigma}_2 - i\partial_y\hat{\sigma}_3,$$
[15]

where σ_i are the three Pauli matrices, and the parameter m is set equal to the inverse decay length (up to a sign) $m = \pm\lambda^{-1}$ such that $\mathcal{H}^2 = (-\nabla^2 + \lambda^{-2})\hat{I}_2$ recovers the original operator up to the 2×2 identity matrix. These correspond to "two copies" of the original operator, which are supersymmetric partners in the quantum interpretation (9). $\mathcal{H}$ has the same zero eigenvector as the original operator other than having a set of pairs of positive and negative eigenvalues, $\pm\sqrt{q_x^2 + q_y^2 + \lambda^{-2}}$, that are proportional to the square roots of the inverse relaxation times of fluctuation modes in the corresponding simple fluids setup. The operator $\mathcal{H}$ thus has "particle-hole" symmetry, but since $\mathcal{H}(q) = -\mathcal{H}^*(-q)$, it breaks time-reversal symmetry and also lacks sublattice symmetry for $\lambda^{-1} \neq 0$ (10, 31). $\mathcal{H}$ is in fact the well-known 2D Dirac Hamiltonian arising in two-band models with an associated Chern number that depends on the sign of the "Dirac mass" m (10, 55), which in our case, corresponds to inverse localization length:

$$\mathcal{C}_\pm = \int \frac{dq_x\, dq_y}{2\pi}\mathcal{F}_\pm = \pm\frac{1}{2}\,\mathrm{sgn}(m),$$
[16]

where $\mathcal{F}_\pm$ is the Berry curvature, a geometric quantity defined in the space of parameters, (q_x, q_y, m), associated with the upper (+) or lower (−) band. Specifically, the Berry curvature of a two-band Hamiltonian, such as given in Eq. **15**, is like the magnetic field of a monopole (10, 55): $\mathcal{F}_\pm = \pm\frac{1}{2}m/(q_x^2 + q_y^2 + m^2)$ (*SI Appendix* has details).

We note that the integrated Berry curvature ("Berry flux") in the bulk here is a half-integer, since the wavenumbers q_x and q_y for a continuous bulk fluid range from $-\infty$ to ∞ instead of being confined to a closed space, such as the Brillouin zone in the case of an underlying lattice. This can, however, still be meaningful, since the difference of Berry flux between two bulk regions with opposite signs of the Dirac mass is an integer (24, 25) that equals the number of modes localized at the interface: $\Delta \mathcal{C}_\pm = \mathcal{C}_\pm(m > 0) - \mathcal{C}_\pm(m < 0) = \pm 1$. Unlike a Chern insulator, such as the electronic Haldane model (56), where the sign of the Dirac mass is determined by the bulk band structure, there is an inherent ambiguity involved in the choice of sign of the mass parameter when constructing the square root as suggested by the operator, $\mathcal{H}$, in Eq. 15. In the bulk, either of $m = \pm \lambda^{-1}$ recovers $\mathcal{H}^2 = -(\nabla^2 - \lambda^{-2})\mathcal{I}_2$. However, given an interface between two bulk regions (such as two regions with different drive), the exponentially localized steady-state edge flows obtained from solving Eq. 13 have to decay away from the interface to their bulk values. This is easy to see for the simple 1D differential operator, which allows exponentially localized zero eigenstates, $\partial_x^2 - \lambda^{-2}$, along the direction normal to an interface (which here is the $x = 0$ line). On either side of the interface, either the growing, $\exp(x/\lambda)$, or the decaying, $\exp(-x/\lambda)$, exponential solution is allowed. This determines the sign of the effective Dirac mass to be opposite in either bulk domain. The importance of an interface may also be seen through the discretized representation of the operator $-(\nabla^2 - \lambda^{-2})$. As discussed in *SI Appendix*, this representation is the square of a topologically nontrivial finite matrix (with a bulk topological index) only for specific choices of boundary conditions. The boundary conditions effectively specify the sign of m in the square root matrix $\mathcal{H}$.

We emphasize that, although for a quantum model and many classical models, the Chern number is associated with the direction of propagation of waves (10, 11, 31) (specifically the difference in the number of right- and left-moving edge modes), such an interpretation is absent in the purely dissipative dynamics that we consider here. The fictitious frequencies (i.e., eigenvalues of $\mathcal{H}$) that we construct here are just the square roots of the inverse relaxation timescales associated with purely diffusive modes (and not propagating waves): $\omega_{eff} = \pm\sqrt{t^{-1}}$. The chirality of the steady-state edge flow itself is not related to the sign of the Chern number but originates from the direction of the driving torque. The topological properties of the model Hamiltonian, which can be derived for certain boundary conditions (as discussed above), guarantee that the steady-state flows and diffusively decaying perturbations about them are robustly localized to the boundary irrespective of the detailed structure of the boundaries.

Topological Properties of Chiral Active Flows. The conclusions outlined above can be easily generalized to the chiral active dynamical operator in Eq. 13. The very long-wavelength normal modes ($q \ll \lambda_{\omega,\Omega}^{-1}$) of the spin–vorticity fluctuations in Eq. 14 are obtained by diagonalizing $\mathbf{M}$ in the small q limit

$$\mathbf{M}_D \simeq - \begin{pmatrix} \bar{D}_S(q^2 + \bar{\lambda}_\Omega^{-2}) & 0 \\ 0 & \bar{D}_T(q^2 + \bar{\lambda}_\omega^{-2}), \end{pmatrix}, \quad [17]$$

where the redefined diffusivities are $\bar{D}_{T,S} = D_{T,S} \mp \Gamma^2 t_d/(\rho\mathcal{I})$ in terms of a timescale associated with the difference in the bulk spectral gaps of the spin and vorticity fluctuations: $t_d^{-1} \equiv (\Gamma + \Gamma_\Omega)/\mathcal{I} - \Gamma_v/\rho$. Each of the two eigenvalues in Eq. 17 has the form $q^2 + \lambda^{-2}$ and by taking square roots as outlined before, can be mapped to a Dirac Hamiltonian (Eq. 15) with corresponding effective Dirac masses: $|m_{\omega,\Omega}| = \lambda_{\omega,\Omega}^{-1}/\sqrt{1 \mp \Gamma^2 t_d/(4\mathcal{I}\rho)}$. Each of these two Dirac Hamiltonians contributes a Berry flux of $\frac{1}{2}\mathrm{sgn}(m_{\omega,\Omega})$ according to Eq. 16. The principle of bulk edge

correspondence when applied to these Dirac Hamiltonians for a chiral edge flow setup ensures the presence of $\Delta \mathcal{C} = 2$ modes localized at the edge. This count of modes predicted by a topological index is consistent with the chiral active hydrodynamic fluctuations being in both spin and vorticity. For linear flow alone, there is only one degree of freedom, the velocity or the vorticity, and the mode count predicts $\Delta \mathcal{C} = 1$ as obtained in the previous section with a single Dirac Hamiltonian. We now show that these protected edge modes, although diffusive, have the special property of having "gapless" dispersions of inverse relaxation timescales.

Bulk Vs. Edge Spectrum of Dissipative Modes. Bulk diffusive modes with dynamics governed by $(\nabla^2 - \lambda^{-2})$, such as in Eq. 17, relax with timescales $t_{bulk}^{-1}(q) \propto (q_x^2 + q_y^2 + \lambda^{-2})$. For concreteness, consider the linearized fluctuations in vorticity alone about the bulk steady state (with uniform spin Ω_b and zero vorticity) of the chiral active hydrodynamics specified by Eq. 13: $\rho\partial_t\omega = (\eta + \Gamma/4)(\nabla^2 - \lambda_\omega^{-2})\omega$. Here, the substrate friction, Γ_v, ensures a "gap" in the fluctuation spectrum of vorticity at $q = 0$, which implies a finite timescale ρ/Γ_v, beyond which velocity fluctuations in the bulk all decay. However, the timescale associated with the relaxation of fluctuations localized near an edge parallel to the y axis (as shown in Fig. 3A) of the form $\delta\omega \sim e^{iq_y y - x/\lambda_\omega}$ is not similarly bounded: $t_{edge}^{-1} = D_T q_y^2$. Here, $D_T = (\nu + \Gamma/4)/\rho$ is the diffusion constant defined before in Eq. 14. This analysis implies that any long-lived fluctuations including the steady-state flow (corresponding to $q_y = 0$) can only be localized at the boundary.

The distinction in the relaxation of bulk and edge modes is a consequence of topological protection, distinct from the propagating wave-like edge modes in quantum and classical dynamics that are not purely dissipative. We again note that, while the dissipative edge modes are topologically protected as described above, the chirality of the edge flow of rotors results directly from the sense of the driving torque and is not a consequence of the topology.

A representative spectrum of inverse timescales of dissipative modes is plotted in Fig. 3B. In the weak spin–vorticity coupling $\Gamma \ll \eta$ regime, these separate into mainly spin (red lines in Fig. 3B) and mainly vorticity (blue lines in Fig. 3B) fluctuations. The solid curves in Fig. 3B indicate the bulk spectra, whereas the dashed lines in Fig. 3B correspond to diffusive long-lived fluctuation modes of spin and vorticity that are localized at the edge and are compatible with stress-free boundary conditions. At $q_y = 0$, these close the gap and correspond to the two linearly independent steady-state solutions of the chiral active flow (22) obtained in *SI Appendix*.

Although we ignored the convective term in our discussion so far, we point out now that its presence does not preclude the topological properties of the diffusive hydrodynamic operator. When perturbed about a uniform flow state, $v_0\hat{y}$, the convective term contributes a term $iv_0 q_y$ to the diagonal elements of $\mathbf{M}$ introduced in Eq. 14, making it non-Hermitian. However, this does not affect the spectral gap at $q = 0$, and therefore, the associated topological protection is still maintained.

Finally, we note the role played by the coupling of spin and vorticity in our analysis. The spin–vorticity coupling, Γ, "mixes" fluctuations in Ω and ω to order $\mathcal{O}(q^2)$ but is not crucial for maintaining the gap. Interestingly, in the absence of substrate friction, although the vorticity spectrum is ungapped, a finite spin–vorticity coupling $\Gamma > 0$ can maintain the gap in the spin fluctuations by dissipating from the spin to the linear degree of freedom.

Molecular Simulations of Driven Rotors. As another test of these ideas, we set up molecular dynamics simulations of a system composed of driven rotors confined in a box. It has been

well-established that the hydrodynamic equations in Eq. **14** are good descriptors of the dynamics of such rotor systems (22, 23). The equations of motion of individual rotors in our molecular dynamics simulations are

$$m\ddot{\mathbf{r}}_i = -\Gamma_v \mathbf{r}_i - \partial_{r_i} \sum_{i \neq j} V(\mathbf{r}_j - \mathbf{r}_i, \theta_i, \theta_j) + \eta_1(t),$$

$$I\ddot{\theta} = \tau - \gamma_\Omega \dot{\theta}_i - \partial_{\theta_i} \sum_{i \neq j} \mathcal{V}(\mathbf{r}_j - \mathbf{r}_i, \theta_i, \theta_j) + \eta_2(t), \quad \textbf{[18]}$$

where Γ_v is the substrate friction, γ_Ω is the rotational friction, τ is the applied torque, $\eta_1(t), \eta_2(t)$ are delta function-correlated Gaussian random variables, and the interaction potentials V are derived from the Yukawa pair potential (23). The detailed parameters used for the simulations are described in *Materials and Methods*.

To check for the existence of localized vorticity predicted by the theory, we computed the time-averaged velocities of the center of mass of the rotors. As is clear from Fig. 4*A*, this system supports localized edge flows. This flow is immune to backscattering in the presence of obstacles and persists even if the edges

of the box used in the simulation are jagged (as depicted in Fig. 4*C*). When the rotors are actively driven only in a partial region of the simulation box (Fig. 4*B*), the flow is localized at the boundary of this region of driving. This may be experimentally realized, for example, in the light-powered micromotors studied in ref. 46 by selectively shining light in the region of interest.

According to a solution of the hydrodynamic equations with a specific choice of boundary conditions (23) (*SI Appendix*), one expects the inverse effective localization length κ to scale like $\kappa^2 \propto \Gamma_v$. This solution and the theoretical analysis above predict a loss of topological protection at zero substrate friction. In agreement with these predictions, the boundary flow velocity continues to be robustly localized as substrate friction Γ_v is reduced until very small values of friction, when the flow profile turns noisy (Fig. 4*D*). The loss of topological protection in a finite system at nonzero friction can be interpreted as a signature of the narrowing of the associated gap in the eigenvalue spectrum of flow solutions in relation to fluctuations as friction is decreased, resulting eventually in an unstable steady state. Similar features are apparent as topological protection is lost in finite-sized electronic and mechanical topological insulator models (57). These
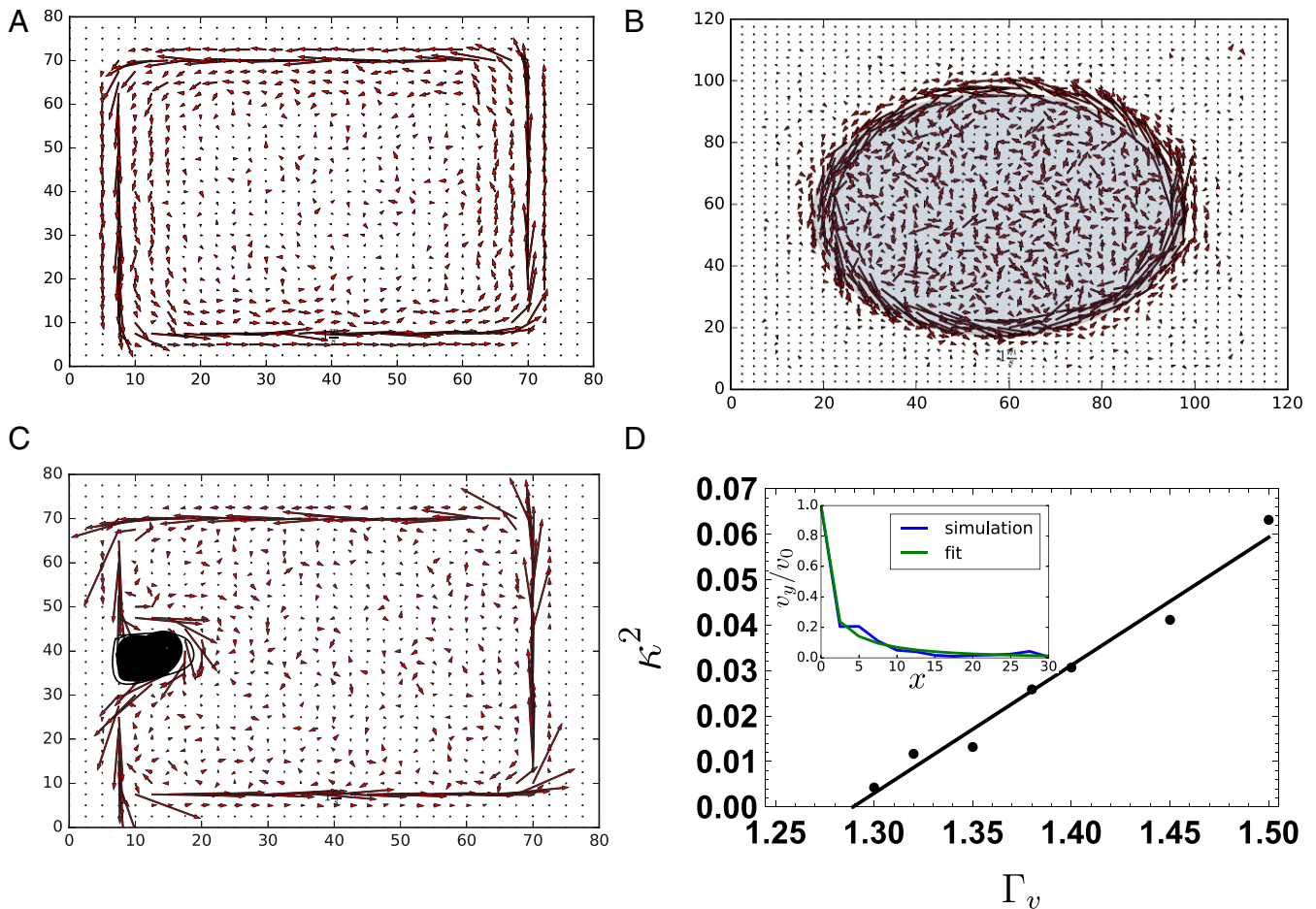

Fig. 4. Edge flows in a collection of driven rotors confined by wall potential. Simulated edge flows in slab geometry. (*A*) Unperturbed boundaries. (*B*) Rotors are driven in a finite subregion (shaded) of the simulation box, illustrating flow localized at the interface of the "active" and "passive" regions. (*C*) Robust flow around an obstacle, showing lack of backscattering. The sizes of the arrows are proportional to the magnitudes of the average velocity, and the directions of the arrows indicate the direction of the flow. The equations of motion used to simulate the rotors are described in Eq. **18** in the text. The bulk dynamics of such rotors is well-described by a hydrodynamic description derived from irreversible thermodynamics. *D* shows increased localization as the substrate friction, Γ_v, is increased. κ is an effective inverse localization length obtained from fitting the simulated velocity profile (shown in *Inset*, where the blue curve is the simulated velocity profile and the green curve is the fit function) to an effective exponential profile. The axes in *Inset* are normalized by the box size L and the maximum edge velocity v_0.

observations taken together constitute a demonstration of the robustness of edge flows to boundary perturbations.

Topological Protection of Propagating Sound Modes. In this paper, we focus on dissipation-dominated processes and topologically interpret the bulk and edge fluctuation spectrum of chiral active hydrodynamics. Even if inertial terms were present in these hydrodynamic equations, the gap in the imaginary (dissipative) part of the spectrum of fluctuation relaxation times inherent in Eq. **14** is preserved. However, the presence of density fluctuations coupled to the longitudinal component of velocity can, in principle, allow propagating sound waves with gapped frequency spectrum (26). By relaxing the incompressibility constraint and perturbing around a uniform edge velocity $\mathbf{v_0}$, we show in *SI Appendix* that sound modes can propagate in the regime of wavenumbers: $\Gamma_v/(\rho_0 v_0) \ll q \ll c/\eta$ for chiral active flows. These are approximately described by the wave equation

$$((\partial_t + \mathbf{v_0} \cdot \nabla)^2 - c^2 \nabla^2)\rho = 0, \qquad [19]$$

which in the limit that the background flow velocity is much lower than sound wave speed $v_0 \ll c$, gives $[(\nabla - i\mathbf{A})^2 + \omega^2/c^2]\tilde{\rho} = 0$, where $\tilde{\rho}(\mathbf{x}, \omega)$ is the density in frequency space and $\mathbf{A} = \omega \mathbf{v_0}/c^2$ is an effective vector potential created by the background edge flow. This gauge field suggests a geometric phase and nontrivial topological properties when the fluid is confined in a lattice geometry. Note that the dissipative spin–vorticity coupling, Γ, is crucial for ensuring a nonzero edge velocity $\mathbf{v_0}$ and hence, a nontrivial topology. The linearized equations describing the sound modes in chiral active flows that we find in *SI Appendix* are in fact isomorphic to those found for sound in polar active flows derived from Toner-Tu active hydrodynamics (26). This implies the existence of topologically protected sound modes for chiral active flows when placed in the microfluidic lattice setup proposed in ref. 26 if the rotors are driven in opposite senses in neighboring cells.

Discussion

Using two disparate examples of complex dynamical systems that are out of equilibrium, we have shown in this paper that topologically protected states can arise in principle in a variety of dissipative systems: both stochastic networks and active flows. Unlike other systems for which topological protection has been previously explored, such as mechanical lattices (9) or propagating sound modes in hydrodynamic equations (25, 26), dissipation is key to the phenomena considered here. In both cases considered, the topological properties are not readily apparent from the structure of the relevant operators that govern their dynamics. We reveal their topological properties by decomposing them suitably to map the properties of their steady-state solutions to the zero-energy states of Hamiltonian models that can be characterized by a topological index. Our work indicates that both single- and many-particle dynamics with interactions at both microscopic and macroscopic scales can result in topological modes that are localized at boundaries. Furthermore, our results also suggest that the chiral edge flows ubiquitously seen in synthetic and biological matter are potentially robust, topologically protected modes. This has applications for self-assembly of metamaterials and can also guarantee robust localized flows of both information and matter in biology.

Materials and Methods

The molecular dynamics simulations were performed by evolving the Langevin equation with Euler dynamics. The rotors in our simulations were composite particles composed of three equally spaced point particles arranged along a line. The particles interact according to a Yukawa potential with a decay length $2d$, where d is the spacing between the particles in the rotor. This force field was used to derive the interatomic forces and torques on the rotor. We set $\Gamma_v = \gamma \Omega$ as the substrate friction. The simulations in Fig. 4 *A*, *C*, and *D* were performed with $N = 160$ particles in a 2D square box with length $L = 80$. The size of the rotors is $d = 2.5$. The charge on the rotors (for the Yukawa potential) was set to $q = 2.5$. The simulations in Fig. 4*B* were performed with $N = 362$ particles in a box with size $L = 120$. The applied torque τ in all of the simulations was $\tau = 10$.

1. Hopfield JJ (1974) Kinetic proofreading: A new mechanism for reducing errors in biosynthetic processes requiring high specificity. *Proc Natl Acad Sci USA* 71:4135–4139.
2. Wang F, et al. (2017) Non-equilibrium effect in the allosteric regulation of the bacterial flagellar switch. *Nat Phys* 13:710–714.
3. Tu Y (2008) The nonequilibrium mechanism for ultrasensitivity in a biological switch: Sensing by Maxwell's demons. *Proc Natl Acad Sci USA* 105:11737–11741.
4. Lan G, Sartori P, Neumann S, Sourjik V, Tu Y (2012) The energy-speed-accuracy tradeoff in sensory adaptation. *Nat Phys* 8:422–428.
5. Cao Y, Wang H, Ouyang Q, Tu Y (2015) The free-energy cost of accurate biochemical oscillations. *Nat Phys* 11:772–778.
6. Barato AC, Seifert U (2015) Thermodynamic uncertainty relation for biomolecular processes. *Phys Rev Lett* 114:158101.
7. Gingrich TR, Horowitz JM, Perunov N, England JL (2016) Dissipation bounds all steady-state current fluctuations. *Phys Rev Lett* 116:120601.
8. Nguyen M, Vaikuntanathan S (2016) Design principles for nonequilibrium self-assembly. *Proc Natl Acad Sci USA* 113:14231–14236.
9. Kane CL, Lubensky TC (2013) Topological boundary modes in isostatic lattices. *Nat Phys* 10:39–45.
10. Hasan MZ, Kane CL (2010) Colloquium: Topological insulators. *Rev Mod Phys* 82:3045–3067.
11. Haldane FDM, Raghu S (2008) Possible realization of directional optical waveguides in photonic crystals with broken time-reversal symmetry. *Phys Rev Lett* 100:013904.
12. Süsstrunk R, Huber SD (2015) Observation of phononic helical edge states in a mechanical topological insulator. *Science* 349:47–50.
13. Nash LM, et al. (2015) Topological mechanics of gyroscopic metamaterials. *Proc Natl Acad Sci USA* 112:14495–14500.
14. Paulose J, Chen BGg, Vitelli V (2015) Topological modes bound to dislocations in mechanical metamaterials. *Nat Phys* 11:153–156.
15. Ryu S, Hatsugai Y (2002) Topological origin of zero-energy edge states in particle-hole symmetric systems. *Phys Rev Lett* 89:077002.
16. Chen BGg, Upadhyaya N, Vitelli V (2014) Nonlinear conduction via solitons in a topological mechanical insulator. *Proc Natl Acad Sci USA* 111:13004–13009.
17. Lubensky TC, Kane CL, Mao X, Souslov A, Sun K (2015) Phonons and elasticity in critically coordinated lattices. *Rep Prog Phys* 78:073901.
18. Callan CG, Freed D (1992) Phase diagram of the dissipative Hofstadter model. *Nucl Phys B* 374:543–566.
19. Rudner MS, Levitov LS (2009) Topological transition in a non-hermitian quantum walk. *Phys Rev Lett* 102:065703.
20. Cayssol J, Dora B, Simon F, Moessner R (2013) Floquet topological insulators. *Phys Status Solidi Rapid Res Lett* 7:101–108.
21. Murugan A, Huse DA, Leibler S (2014) Discriminatory proofreading regimes in nonequilibrium systems. *Phys Rev X* 4:021016.
22. Tsai JC, Ye F, Rodriguez J, Gollub JP, Lubensky TC (2005) A chiral granular gas. *Phys Rev Lett* 94:214301.
23. van Zuiden BC, Paulose J, Irvine WTM, Bartolo D, Vitelli V (2016) Spatiotemporal order and emergent edge currents in active spinner materials. *Proc Natl Acad Sci USA* 113:12919–12924.
24. Delplace P, Marston JB, Venaille A (2017) Topological origin of equatorial waves. *Science* 358:1075–1077.
25. Shankar S, Bowick MJ, Marchetti MC (2017) Topological sound and flocking on curved surfaces. *Phys Rev X* 7:031039.
26. Souslov A, van Zuiden BC, Bartolo D, Vitelli V (2017) Topological sound in active-liquid metamaterials. *Nat Phys* 13:1091–1094.
27. Schnakenberg J (1976) Network theory of microscopic and macroscopic behavior of master equation systems. *Rev Mod Phys* 48:571–585.
28. Van Kampen N (2011) *Stochastic Processes in Physics and Chemistry* (Elsevier Science, Amsterdam).
29. Su WP, Schrieffer JR, Heeger AJ (1979) Solitons in polyacetylene. *Phys Rev Lett* 42:1698–1701.
30. Murugan A, Vaikuntanathan S (2017) Topologically protected modes in non-equilibrium stochastic systems. *Nat Commun* 8:13881.

APPLIED PHYSICAL SCIENCES

31. Süsstrunk R, Huber SD (2016) Classification of topological phonons in linear mechanical metamaterials. *Proc Natl Acad Sci USA* 113:E4767–E4775.
32. Jack RL, Sollich P (2009) Duality symmetries and effective dynamics in disordered hopping models. *J Stat Mech Theory Exp* 2009:P11011.
33. Murugan A, Huse DA, Leibler S (2012) Speed, dissipation, and error in kinetic proofreading. *Proc Natl Acad Sci USA* 109:12034–12039.
34. Murugan A, Vaikuntanathan S (2016) Biological implications of dynamical phases in non-equilibrium networks. *J Stat Phys* 162:1183–1202.
35. Mehta P, Schwab DJ (2012) Energetic costs of cellular computation. *Proc Natl Acad Sci USA* 109:17978–17982.
36. Lebowitz J, Spohn H (1999) A Gallavotti–Cohen-type symmetry in the large deviation functional for stochastic dynamics. *J Stat Phys* 95:333–365.
37. Ichiki A, Ohzeki M (2013) Violation of detailed balance accelerates relaxation. *Phys Rev E* 88:020101.
38. Kaiser M, Jack RL, Zimmer J (2017) Acceleration of convergence to equilibrium in Markov chains by breaking detailed balance. *J Stat Phys* 168:259–287.
39. Cates ME, Tailleur J (2015) Motility-induced phase separation. *Annu Rev Condens Matter Phys* 6:219–244.
40. del Junco C, Tociu L, Vaikuntanathan S (2016) Energy dissipation and fluctuations in a driven liquid. *Proc Natl Acad Sci USA* 115:3569–3574.
41. Marchetti MC, et al. (2013) Hydrodynamics of soft active matter. *Rev Mod Phys* 85:1143–1189.
42. Kruse K, Joanny JF, Jülicher F, Prost J, Sekimoto K (2005) Generic theory of active polar gels: A paradigm for cytoskeletal dynamics. *Eur Phys J E Soft Matter* 16:5–16.
43. Whitelam S, Schulman R, Hedges L (2012) Self-assembly of multicomponent structures in and out of equilibrium. *Phys Rev Lett* 109:265506.
44. Nguyen NHP, Klotsa D, Engel M, Glotzer SC (2014) Emergent collective phenomena in a mixture of hard shapes through active rotation. *Phys Rev Lett* 112:075701.
45. Migler KB, Meyer RB (1991) Solitons and pattern formation in liquid crystals in a rotating magnetic field. *Phys Rev Lett* 66:1485–1488.
46. Maggi C, Saglimbeni F, Dipalo M, De Angelis F, Di Leonardo R (2015) Micromotors with asymmetric shape that efficiently convert light into work by thermocapillary effects. *Nat Commun* 6:7855.
47. Fürthauer S, Strempel M, Grill SW, Jülicher F (2013) Active chiral processes in thin films. *Phys Rev Lett* 110:048103.
48. Naganathan SR, Fürthauer S, Nishikawa M, Jülicher F, Grill SW (2014) Active torque generation by the actomyosin cell cortex drives left-right symmetry breaking. *eLife* 3:e04165.
49. de Groot S, Mazur P (1969) *Non-Equilibrium Thermodynamics* (North-Holland, Amsterdam).
50. Fürthauer S, Strempel M, Grill SW, Jülicher F (2012) Active chiral fluids. *Eur Phys J E* 35:89.
51. Mandal D, Klymko K, Mandadapu KK (2017) Generalized hydrodynamics of active polar suspensions. arXiv:1706.02284v1.
52. Klymko K, Mandal D, Mandadapu KK (2017) Statistical mechanics of transport processes for active fluids: Equations of hydrodynamics. arXiv:1706.02694.
53. Banerjee D, Souslov A, Abanov AG, Vitelli V (2017) Odd viscosity in chiral active fluids. *Nat Commun* 8:1573.
54. Dirac PAM (1928) The quantum theory of the electron. *R Soc Lond Proc A* 117:610–624.
55. Asbóth JK, Oroszlány L, Pályi A (2016) *A Short Course on Topological Insulators, Lecture Notes in Physics* (Springer, New York).
56. Haldane FDM (1988) Model for a quantum hall effect without landau levels: Condensed-matter realization of the "parity anomaly." *Phys Rev Lett* 61:2015–2018.
57. Rocklin DZ, Chen BG, Falk M, Vitelli V, Lubensky TC (2016) Mechanical weyl modes in topological maxwell lattices. *Phys Rev Lett* 116:135503.